APL Materials

RESEARCH ARTICLE | MAY 30 2024

Reciprocal space x-ray computed tomography

Arturas Vailionis ; Liyan Wu ; Jonathan E. Spanier

APL Mater. 12, 051128 (2024)
https://doi.org/10.1063/5.0203995

Reciprocal space x-ray computed tomography

Cite as: APL Mater. 12, 051128 (2024); doi: 10.1063/5.0203995
Submitted: 18 February 2024 • Accepted: 7 May 2024 •
Published Online: 30 May 2024

Arturas Vailionis,[1,2,a] Liyan Wu,[3,4] and Jonathan E. Spanier[3,4]

AFFILIATIONS

[1] Stanford Nano Shared Facilities, Stanford University, Stanford, California 94305, USA
[2] Department of Physics, Kaunas University of Technology, LT-51368 Kaunas, Lithuania
[3] Department of Mechanical Engineering and Mechanics, Drexel University, Philadelphia, Pennsylvania 19104, USA
[4] Department of Materials Science and Engineering, Drexel University, Philadelphia, Pennsylvania 19104, USA

[a] Author to whom correspondence should be addressed: a.vailionis@stanford.edu

ABSTRACT

Three-dimensional reciprocal space mapping (3D-RSM) offers crucial insights into the intricate microstructural properties of materials, including spatial domain distribution, directional long-range ordering, multilayer-substrate mismatch, layer tilting, and defect structure. Traditionally, 3D-RSMs are conducted at synchrotron facilities where instrumental resolution is constrained in all three directions. Lab-based sources have often been considered suboptimal for 3D-RSM measurements due to poor instrumental resolution along the axial direction. However, we demonstrate that, by employing three-dimensional reciprocal space x-ray computed tomography (RS-XCT), the same perceived limitation in resolution can be effectively leveraged to acquire high quality 3D-RSMs. Through a combination of ultrafast reciprocal space mapping and computed tomography reconstruction routines, lab-based 3D-RSMs achieve resolutions comparable to those obtained with synchrotron-based techniques. RS-XCT introduces a practical modality for lab-based x-ray diffractometers, enabling high-resolution 3D-RSM measurements on a variety of materials exhibiting complex three-dimensional scattering landscapes in reciprocal space.

Reciprocal space mapping (RSM) is a widely used x-ray diffraction technique that enables the resolution of Bragg peaks, their shapes, the locations of tilted structural domains, and diffuse scattering features in a three-dimensional reciprocal space.[1,2] The method typically necessitates a well-defined instrumental resolution—smaller than the features one intends to observe in reciprocal space. The resolution of the x-ray diffractometer is determined by factors such as the divergence of the incident and diffracted x-ray beams, as well as the energy spread of the x-rays. The resolution can be visually represented as a scattering vector with a blunted tip.

In x-ray diffraction, the scattering vector is defined by the following equation:

$$S = k_h - k_0 = \frac{s - s_0}{\lambda}, \tag{1}$$

where s and s_0 are the unit vectors, k_h and k_0 are the wave vectors, and λ is the x-ray wavelength. As the scattering vector coincides with the reciprocal lattice point, Bragg's law is satisfied. This is schematically shown in Fig. S1 (see the supplementary material). The figure illustrates real space with the incident and diffracted beams and atomic planes, while reciprocal space is represented by the scattering vector, origin point (000), and reciprocal lattice point $\mathbf{d}^*(hkl)$. The various Bragg peaks and scattering features around them can be accessed in the 3D reciprocal space by utilizing a four-circle goniometer. The angles of the four-circle goniometer cradle are shown in Fig. 1(a).

In an ideal situation and within the kinematical scattering approximation, the reciprocal lattice point of a perfect, "infinitely" thick single crystal forms a single, sharp point with no width, and the scattering vector is infinitely precise. In reality, however, the reciprocal lattice point exhibits broadening along specific directions, containing essential structural information such as finite layer thickness, mosaicity, variation in d-spacing, and more. Reciprocal space mapping serves as a highly effective tool for identifying the broadening of Bragg peaks along all three dimensions. Furthermore, reciprocal space is also populated by off Bragg peak scattering features stemming from phenomena such as crystal truncation,[3] waviness of the atomic planes,[4] ferroelectric domain distribution,[5] and other factors closely related to the material's physical properties.

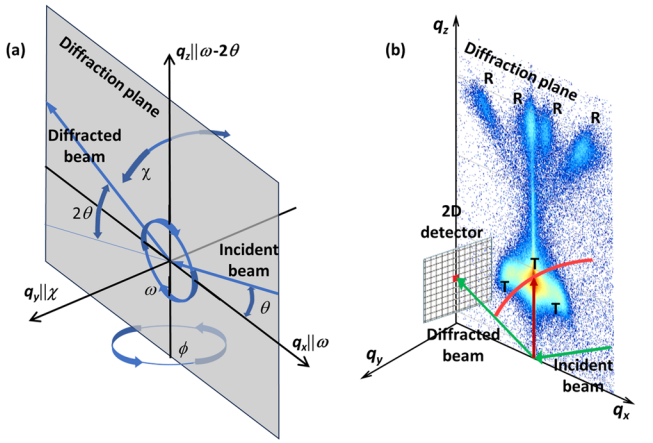

FIG. 1. (a) Schematic drawing of the coordinate system of a four-circle goniometer depicting angles of the diffractometer. The diffraction plane is the q_x–q_z plane. The statements $q_x||\omega$ and $q_y||\chi$ are only valid within small angles of rotation, where the rotations along ω and χ arches can be approximated as straight lines. (b) Visual representation of two-dimensional reciprocal space mapping of the mixed-phase $BiFeO_3$ layer near the $LaAlO_3$(001) Bragg diffraction peak using a laboratory-based line-focused x-ray beam and a 2D detector. The $BiFeO_3$ highly strained tetragonal-like phase (T-phase) Bragg peak and its tilted variants, as well as four peaks of highly strained R-phase, are marked for clarity. The peak notations were taken from Ref. 14. The scattering vector is shown as a red arrow, and its end is shown as a red arch line that is sharp within the diffraction plane but significantly elongated along the χ-direction. The total scattering intensity along the scattering vector arch in the q_y direction is represented by a single pixel of the 2D detector.

In lab-based diffractometers, the x-ray beam is typically employed in a configuration known as "line focus." In this setup, both the x-ray beam and the x-ray optics limit the beam divergence within a two-dimensional diffraction plane. For instance, a combination of a parabolic Goebel mirror and a two-bounce asymmetrical Ge(220) beam conditioner on the incident beam side yields a monochromatic $K\alpha_1$ beam with a divergence of ~25 arcsec along the omega direction. When this is combined with a Ge(220) channel analyzer crystal on the diffracted beam side, the scattering vector, or x-ray probe, exhibits an angular spread of around 25 × 25 arcsec within the diffraction plane. However, in the axial direction, the lab-based and line-focused x-ray beam has a significantly wider divergence, resulting in a relatively large angular length of the x-ray probe. The typical lab-based instrument's resolution is shown in Fig. S2 of the supplementary material. Here, we see that within the diffraction plane, the broadening of the single crystal Si(004) peak is relatively small. Along the ω-2θ direction, peak broadening is mainly determined by the resolution of the incident beam optics [in this case, the Goebel mirror with a Ge(220) two-bounce beam conditioner]. Along the 2θ direction, the beam is additionally broadened by the incident beam footprint on the sample, which highly depends on the angle of incidence and the beam size defined by the divergence slit. The same Si(004) Bragg peak in a plane perpendicular to the diffraction plane looks quite different. The peak intensity along the χ direction extends over 6°, indicating the size of the scattering vector (probe) in that direction.

Such a lab-based x-ray probe is routinely employed for reciprocal space mapping, as shown in Fig. 1(b). If the Bragg peaks and off Bragg peak scattering features are well-defined and adequately separated in reciprocal space, a two-dimensional reciprocal space map (2D-RSM) provides essential structural information related to mosaicity, d-spacing variation, domain orientation, and long-range ordering.

In certain cases, reciprocal space exhibits a high density of intricately arranged features along both equatorial and axial directions. A notable example is epitaxial $BiFeO_3$ layers, where 2D-RSMs reveal complicated patterns of multiple highly strained ferroelectric domains distributed across all three directions in the reciprocal space.[6,7] Interpreting such 2D-RSMs can be challenging, making three-dimensional x-ray reciprocal space mapping (3D-RSM) an essential tool. At present, 3D-RSM is typically conducted at synchrotron facilities, where the x-ray beam divergence can be constrained in both equatorial and axial directions.[8,9] Equatorial beam divergence determines the instrument resolution within the diffraction plane, while axial divergence defines the resolution perpendicular to the diffraction plane.

In this study, we demonstrate the successful and relatively fast acquisition of high quality 3D-RSMs using a 3rd generation Malvern Panalytical Empyrean laboratory-based x-ray diffractometer, which boasts high resolution within the diffraction plane but has a wide acceptance angle along the axial direction (χ-axis in a four-circle goniometer). By employing a combination of ultrafast RSM data acquisition, image enhancement, and typical computed tomography (CT) reconstruction routines, we were able to obtain three-dimensional reciprocal space maps with resolution rivaling that of the synchrotron-based 3D-RSMs in all three directions and only limited by the resolution within a diffraction plane.

As shown in Fig. 1(b), the 2D-RSM obtained by the lab-based line-focused x-ray beam represents a two-dimensional high-resolution image of x-ray intensity in reciprocal space. Here, we show a two-dimensional reciprocal space map of the mixed-phase $BiFeO_3$ layer near the $LaAlO_3$(001) Bragg diffraction peak.

Each measurement point in the diffraction plane combines intensities along the axial direction within the full detector's acceptance angle along the χ-axis. Therefore, a single 2D-RSM x-ray diffraction image resembles a 2D x-ray transmission image through an object, where each 2D pixel contains cumulative density information of the object along the path of the x-ray beam (the third dimension). In the field of x-ray computed tomography (XCT),[10] a set of such projection images collected at various rotation angles of the object is commonly employed for the tomographic reconstruction of a three-dimensional object volume.[11] In this context, the grayscale level is proportional to the material's density.

In standard XCT, the intensity within each pixel (x, y) of the 2D image is determined by the attenuation of the x-ray beam along the path through the object, following Beer–Lambert's law,

$$I(x,y) = I_0(x,y)\exp\left(-\sum_{i=1}^{n}\mu_i z_i\right), \quad (2)$$

where I_0 is the intensity of the incident beam, μ_i is the linear attenuation coefficient, and z_i is the path length element through the object. For the 2D-RSM image, the intensity at each pixel is defined

by constructive interference of the incident x-ray beam at a particular scattering vector position in the diffraction plane (q_x, q_z) that is summed up along the axial direction, q_y,

$$I(q_x, q_z) = \sum_{y=1}^{n} I\left(q_x, q_z, q_y\right). \tag{3}$$

In this context, the intensity at each pixel, $I_{qx,qz}$, contains comprehensive information about the intensity distribution along the q_y direction, denoted as I_{qy}. If we acquire a sufficient number of 2D-RSM images at different rotation angles, ϕ, we will be able to reconstruct the three-dimensional scattered intensity distribution from the sample in reciprocal space while maintaining the resolution determined by the incident and diffracted beam optics within the diffraction plane.

The method initially described by Meduňa *et al.*[12] utilized a lab-based instrument with comparable resolution to capture 2D-RSM images and reconstruct the 3D volume of reciprocal space using the MATLAB program with a built-in Radon transform function. However, their method faced significant hurdles, particularly in addressing streaking artifacts resulting from undersampling.

In contrast, the modality described here, reciprocal space x-ray computed tomography (RS-XCT), provides an effective solution. By harnessing ultrafast reciprocal space mapping (URSM), coupled with advanced image enhancement techniques and CT reconstruction, RS-XCT excels in generating high-resolution three-dimensional reciprocal space maps using a lab-based x-ray diffractometer. The utilization of URSM enables us to gather a sufficiently large number of projections in a reasonable time, thereby eliminating the aliasing artifacts encountered in Meduňa *et al.*'s methodology. In addition, our incorporation of 2D-RSM image enhancement routines ensures the enhancement of critical features, guaranteeing optimal images for subsequent reconstruction. An example illustrating the effectiveness of image enhancement is depicted in Fig. S3. In addition, we provide a comprehensive description of the detailed steps involved in image enhancement using MATLAB. Furthermore, careful sample orientation at each rotation step, ϕ, guarantees precise alignment of the center of rotation with the primary Bragg peak of the layer. Subsequent center shift adjustments within the Dragonfly's CT Reconstructor refine the reconstruction process, improving the overall accuracy of the reconstructed volume. The detailed workflow of the RS-XCT modality is demonstrated in Fig. S4.

In practical application, our method outperforms other approaches. For instance, when analyzing a $BaTiO_3$ layer, we gathered 500 2D-RSMs over a full 360° rotation in 16.7 h, with a step size of $\Delta\phi$ = 0.72°. The time taken to acquire each 2D-RSM was only 2 min. Similarly, when examining a $BiFeO_3$ layer with widely spaced features in reciprocal space, we acquired 400 2D-RSMs over the same rotation range in 46.7 h with a step size of $\Delta\phi$ = 0.9°. Here, the time taken to acquire each 2D-RSM was 7 min.

While it is true that a 180° rotation is typically sufficient for a satisfactory CT scan, there are specific advantages to extending the rotation to 360°. Research indicates that a 360° acquisition provides more comprehensive Fourier spectral information on projection data, leading to more homogeneous images, especially for features located away from the center of rotation.[13] This additional rotational range enhances the accuracy and completeness of the reconstructed volume, particularly for complex samples with distributed features.

However, it is important to note that our proposed modality is versatile and can be successfully employed with a 180° rotation as well. This approach significantly accelerates the RSM-CT data collection process, effectively halving the acquisition time with only a minor reduction in final 3D volume quality.

All measurements were conducted using a 3rd generation Malvern Panalytical Empyrean x-ray diffractometer, equipped with a hybrid monochromator [comprising a parabolic Goebel mirror and a two-bounce Ge(220) monochromator] on the incident beam

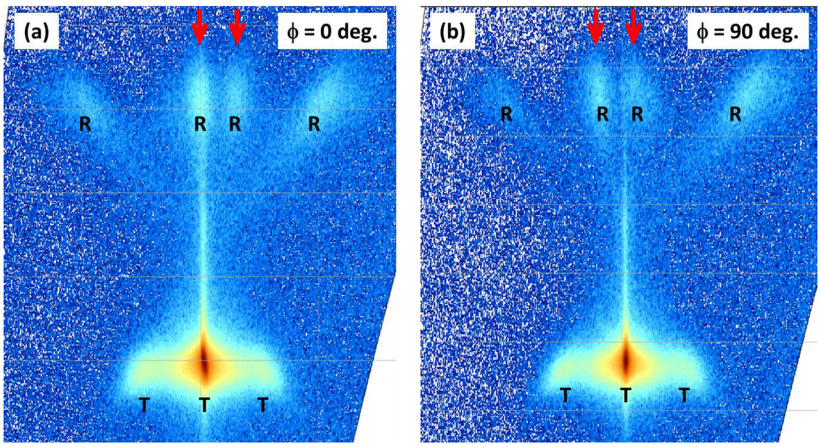

FIG. 2. 2D reciprocal space maps of the mixed-phase $BiFeO_3$ layer near the $LaAlO_3$(001) Bragg diffraction peak. Only highly strained T-phase and R-phase scattering features are shown: (a) at a rotation angle of ϕ = 0° and (b) ϕ = 90°. As the sample is rotated by 90°, observe how peaks from strained R-phase domains, indicated by the red arrows, shift. This movement indicates that these peaks are not confined to the diffraction plane but are instead projected along the axial direction onto the diffraction plane.

side and a 2D GaliPIX^{3D} x-ray detector on the diffracted beam side. Such a setup allows for the rapid acquisition of ultrafast RSMs within a few minutes, making reciprocal space x-ray computed tomography feasible.

In this work, the domain structure of two epitaxial layers was analyzed using RS-XCT: the $BiFeO_3$ layer on the $LaAlO_3$(001) substrate (BFO/LAO) and the $BaTiO_3$ layer on the $NdScO_3$(110) substrate (BTO/NSO). The 2D-RSM images were acquired around symmetrical (00*l*) reflections at different ϕ-axis positions.

The 2D-RSMs near the BFO(001) Bragg peak, taken at ϕ angles of 0° and 90°, are shown in Figs. 2(a) and 2(b), respectively. As evident from the figure, the BFO RSMs display a complex scattering pattern, originating from the presence of highly strained R- and T-phases within the BFO layer.[14] Notably, the position of R-phase features near the top center of the RSMs changes as the ϕ angle is rotated from 0° to 90°, indicating that these off Bragg scattering features are not located within the diffraction plane. Indeed, the RSM of similar BFO layers measured using synchrotron sources, where the monochromatic x-ray beam has low divergence in all three directions, does not exhibit features from the BFO R-phase near the top center of the map.[15,16] The maps show only two tilted scattering features from the R-phase at higher tilt angles, which are also visible in lab-based RSM and are consistent with the actual tilting of the R-phase domains.[14–16] Based on these observations, we can conclude that the lab-based 2D-RSMs shown in Fig. 2 represent the summed-up scattering intensity along the direction perpendicular to the diffraction plane. This occurs due to the large acceptance angle of the detector along the χ-direction, and this scattering intensity is projected onto the diffraction plane, making it visible in the 2D-RSM.

The 2D-RSMs around the BTO(002) peak are presented in Figs. 3(a)–3(c), acquired at ϕ = 0°, 45°, and 90°, respectively. As observed from the figures, the distribution of ferroelectric domains in the BTO layer is unidirectional, aligned along the NSO[-110] direction. The intricate scattering pattern around the main BTO(002) Bragg peak visible along the NSO[-110] direction in Fig. 3 is a result of the coexistence of periodic *a* and *c* domains, with domain walls aligned along the NSO[-110] direction. Typically, such patterns are characterized using synchrotron-based 3D-RSM.[17–19] When we rotate the sample ϕ = 45° away from the NSO[-110] direction, we can still observe off Bragg scattering peaks from the domains. However, they appear at different positions, clearly indicating that at this rotation angle, they do not originate from scattering in the diffraction plane. Instead, they are projected from the axial (perpendicular) direction into the diffraction plane. At ϕ = 90°, the scattering from the domains is not evident, as all scattering features are now aligned along the axial direction.

As we rotate the sample around the ϕ axis and collect a new reciprocal space map at each ϕ position, we obtain a series of 2D images of the reciprocal space, each containing information along the perpendicular direction that is projected into the 2D-RSM diffraction plane. Our assertion that each recorded 2D-RSM is a Radon transform holds true if the value at each (q_x, q_z) point is equal to the line integral of the function along the q_y line.

To validate this assumption, we examined the resolution function along the χ direction, which effectively corresponds to the q_y axis in reciprocal space. This is a valid assumption: if χ angle does not vary too much, then χ arch can be approximated by a straight line that is parallel to q_y. As illustrated in Fig. S2, the resolution function along this direction is ~6.4°, corresponding to a Δq_y of 0.52 Å^{-1}. Importantly, the separation of measured features in the reciprocal space for the samples under investigation falls comfortably within this resolution, with Δq_y values of 0.24 Å^{-1} for BFO/LAO and 0.05 Å^{-1} for BTO/NSO. This confirms that our resolution function adequately captures all relevant features along the q_y direction.

Another issue related to successful reconstruction is finding an accurate center of rotation (COR). The incorrect COR would deteriorate the quality of the sinogram and overall reconstruction. The correct COR was ensured in two ways:

- After each sample rotation increment, $\Delta\phi$, an alignment on the main Bragg diffraction peak of the substrate was performed. This ensures that the center of rotation remains parallel to the [00l] direction.
- Prior to reconstruction, additional COR determination was conducted using the CT Reconstructor within the Dragonfly software, employing one of the following COR routines:
  - Tomopy Nghia Vo.[20]
  - Tomopy Image Entropy Error.[21]
  - Tomopy Phase Correlation in Fourier Space.[22]

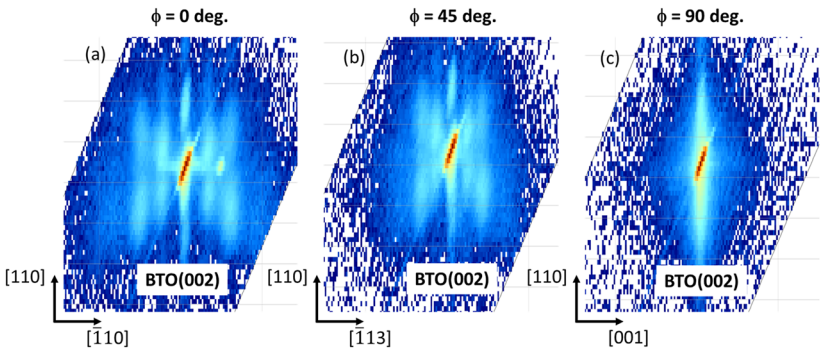

FIG. 3. 2D reciprocal space maps of the $BaTiO_3$ layer grown on the $NdScO_3$(110) substrate. Only layer $BaTiO_3$(002) Bragg peak and scattering features originating from tilted periodic a/c domains are shown: (a) at a rotation angle of ϕ = 0°, (b) ϕ = 45°, and (c) ϕ = 90°.

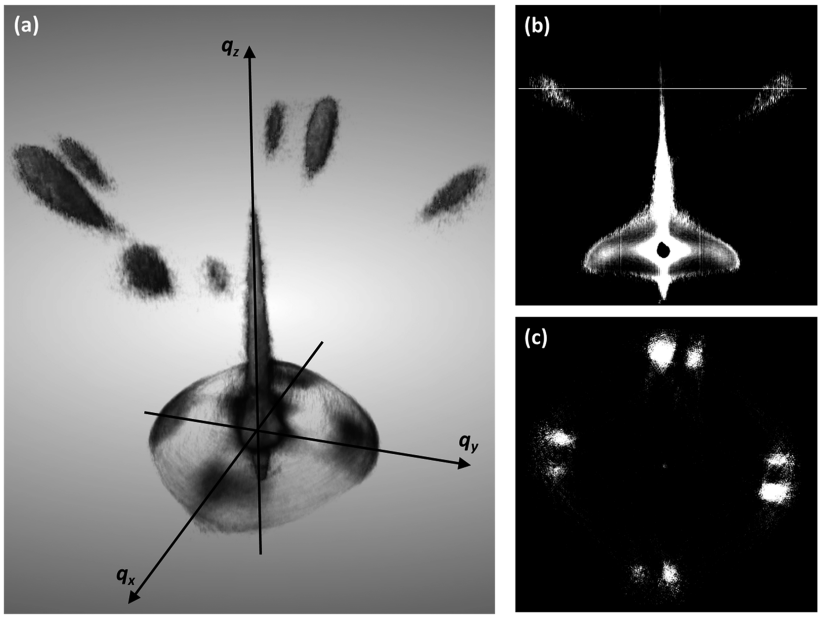

FIG. 4. RS-XCT of the $BiFeO_3$ layer on the $LaAlO_3$(001) single crystal substrate. (a) Rendered 3D-RSM, (b) vertical, and (c) horizontal slices of the 3D-RSM volume. The white line in (b) indicates the horizontal RSM cut shown in (c). Note that the vertical slice does not show R-phase features near the top center visible in Fig. 2.

These methods collectively ensure that the 2D-RSMs acquired at each rotation angle accurately represent the Radon transform of the features in reciprocal space along the q_y direction. Moreover, they guarantee that the sinogram exhibits a continuous variation of intensity in a sine or cosine manner without interruptions, thereby facilitating reliable and robust reconstruction processes.

After gathering the complete dataset spanning the ϕ range of 0°–360°, the 2D-RSM images underwent enhancement using image

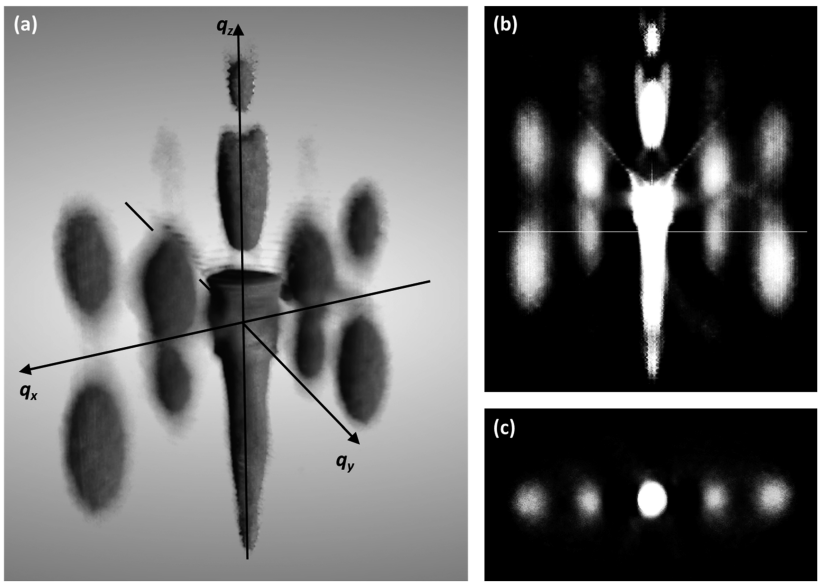

FIG. 5. RS-XCT of the $BaTiO_3$ layer on the $NdScO_3$(110) single crystal substrate. (a) Rendered 3D-RSM, (b) vertical, and (c) horizontal slices of the 3D-RSM volume confirm the uniaxial alignment of the *a* and *c* domain walls. The white line in (b) indicates the horizontal RSM cut shown in (c).

processing tools provided by the MATLAB package. A comprehensive algorithm detailing the image enhancement process is provided in the supplementary material.

Each 2D reciprocal space map can be treated as a 2D projection image, similar to those used in x-ray computed tomography, where the third dimension is projected onto a 2D plane. This allows us to apply the same reconstruction techniques used in XCT. In our case, we utilized the "CT Reconstruction" module for reconstructing parallel-beam projection data into the 3D volume available within the Dragonfly software by Object Research Systems (ORS), Inc. We employed the TomoPy reconstruction engine, which is based on an open-source Python package for tomographic data processing and image reconstruction.[23] We used the "gridrec" Fourier grid reconstruction algorithm.[24]

The general workflow for reciprocal space x-ray computed tomography is illustrated in Fig. S4. With this approach, we successfully reconstructed the 3D reciprocal space volume of both BFO/LAO and BTO/NSO samples. A rendered snapshot of the 3D reciprocal space volume for the BFO/LAO sample is shown in Fig. 4(a). The full rotational movie of the 3D RSM is included in the supplementary material. Figures 4(b) and 4(c) represent vertical and horizontal cuts through the 3D RS volume, respectively. As can be noted from Fig. 4(b), only higher tilt scattering features originating from R-phase domains are observed in the 2D vertical slice. Moreover, a lab-based 3D-RSM can successfully resolve the in-plane rotational split of R-domains visible in Fig. 4(c), confirming that this method achieves a resolution similar to synchrotron-based 3D-RSM.[15,16] The RS-XCT for the BTO/NSO sample is shown in Fig. 5. The vertical and horizontal cuts shown in Figs. 5(b) and 5(c) confirm the unidirectional alignment of the *a* and *c* domain walls. Remarkably, despite the fact that the lab-based x-ray probe's resolution along the axial direction is poor, the resolution achieved in 3D-RSM along the axial direction is similar to that of the diffraction plane. This is corroborated by the similar size of scattering features along the axial and equatorial directions, visible in Fig. 5(c).

In summary, we have introduced a practical technique that harnesses the power of ultrafast reciprocal space mapping, image enhancement, and CT reconstruction to generate high-resolution 3D visualizations of x-ray scattering in reciprocal space using a conventional lab-based x-ray diffractometer. The resolution achieved in the reciprocal space rivals that of synchrotron-based 3D-RSM, signifying the effectiveness of lab-based RS-XCT. We believe that this technique holds promise for a wide range of applications, particularly in scenarios where reciprocal space features are complex and distributed throughout three-dimensional space.

See the supplementary material for the following: Figs. S1–S4 and Movies S1 and S2.

The authors acknowledge H. Christen for providing the $BiFeO_3/LaAlO_3$ sample. Part of this work was performed at the Stanford Nano Shared Facilities (SNSF), supported by the National Science Foundation under Award No. ECCS-2026822. L.W. and J.E.S. acknowledge the support from the U.S. Army Research Laboratory via the Collaborative for Hierarchical, Agile, and Responsive Materials (CHARM) under Cooperative Agreement No. W911NF-19-2-0119 and from the U.S. Army Research Office under Grant No. W911NF-21-1-0126.

AUTHOR DECLARATIONS

Conflict of Interest

The authors have no conflicts to disclose.

Author Contributions

A.V. conceptualized the idea, L.W. and J.E.S. synthesized the samples, A.V. and L.W. performed x-ray diffraction measurements, A.V. carried out data analysis and visualization, A.V. wrote the manuscript and all authors contributed to the writing.

Arturas Vailionis: Conceptualization (equal); Funding acquisition (equal); Investigation (equal); Methodology (equal); Validation (equal); Visualization (equal); Writing – original draft (equal); Writing – review & editing (equal). **Liyan Wu**: Formal analysis (equal); Methodology (supporting); Writing – review & editing (equal). **Jonathan E. Spanier**: Funding acquisition (equal); Methodology (equal); Resources (equal); Writing – review & editing (equal).

DATA AVAILABILITY

The data that support the findings of this study are available within the article and its supplementary material.

REFERENCES

[1] P. F. Fewster, J. Appl. Crystallogr. **22**, 64 (1989).
[2] P. F. Fewster, Appl. Surf. Sci. **50**, 9 (1991).
[3] I. K. Robinson, Phys. Rev. B **33**, 3830 (1986).
[4] A. Vailionis, H. Boschker, W. Siemons, E. P. Houwman, D. H. A. Blank, G. Rijnders, and G. Koster, Phys. Rev. B **83**, 064101 (2011).
[5] D. D. Fong, G. B. Stephenson, S. K. Streiffer, J. A. Eastman, O. Auciello, P. H. Fuoss, and C. Thompson, Science **304**, 1650 (2004).
[6] R. J. Zeches, M. D. Rossell, J. X. Zhang, A. J. Hatt, Q. He, C. H. Yang, A. Kumar, C. H. Wang, A. Melville, C. Adamo, G. Sheng, Y. H. Chu, J. F. Ihlefeld, R. Erni, C. Ederer, V. Gopalan, L. Q. Chen, D. G. Schlom, N. A. Spaldin, L. W. Martin, and R. Ramesh, Science **326**, 977 (2009).
[7] H. M. Christen, J. H. Nam, H. S. Kim, A. J. Hatt, and N. A. Spaldin, Phys. Rev. B **83**, 144107 (2011).
[8] S. O. Mariager, C. M. Schleputz, M. Aagesen, C. B. Sorensen, E. Johnson, P. R. Willmott, and R. Feidenhans'l, Phys. Status Solidi A **206**, 1771 (2009).
[9] S. Bauer, S. Lazarev, M. Bauer, T. Meisch, M. Caliebe, V. Holy, F. Scholz, and T. Baumbach, J. Appl. Crystallogr. **48**, 1000 (2015).
[10] P. J. Withers, C. Bouman, S. Carmignato, V. Cnudde, D. Grimaldi, C. K. Hagen, E. Maire, M. Manley, A. Du Plessis, and S. R. Stock, Nat. Rev. Methods Primers **1**, 18 (2021).
[11] G. Currie, J. Hewis, and S. Bushong, J. Med. Imaging Radiat. Sci. **46**, 403 (2015).
[12] M. Meduňa, F. Isa, F. Bressan, and H. von Känel, J. Appl. Crystallogr. **55**, 823 (2022).
[13] Y.-H. Liu, P. T. Lam, A. J. Sinusas, and F. J. Th. Wackers, J. Nucl. Med. **43**, 1115 (2002).
[14] Q. He, Y. H. Chu, J. T. Heron, S. Y. Yang, W. I. Liang, C. Y. Kuo, H. J. Lin, P. Yu, C. W. Liang, R. J. Zeches, W. C. Kuo, J. Y. Juang, C. T. Chen, E. Arenholz, A. Scholl, and R. Ramesh, Nat. Commun. **2**, 225 (2011).
[15] Z. Chen, S. Prosandeev, Z. L. Luo, W. Ren, Y. Qi, C. W. Huang, L. You, C. Gao, I. A. Kornev, T. Wu, J. Wang, P. Yang, T. Sritharan, L. Bellaiche, and L. Chen, Phys. Rev. B **84**, 094116 (2011).
[16] Z. L. Luo, H. Huang, H. Zhou, Z. H. Chen, Y. Yang, L. Wu, C. Zhu, H. Wang, M. Yang, S. Hu, H. Wen, X. Zhang, Z. Zhang, L. Chen, D. D. Fong, and C. Gao, Appl. Phys. Lett. **104**, 182901 (2014).

[17]M. Schmidbauer, L. Bogula, B. Wang, M. Hanke, L. von Helden, A. Ladera, J.-J. Wang, L.-Q. Chen, and J. Schwarzkopf, J. Appl. Phys. **128**, 184101 (2020).
[18]K. Lee, H. Yi, W.-H. Park, Y. K. Kim, and S. Baik, J. Appl. Phys. **100**, 051615 (2006).
[19]G. Catalan, A. Lubk, A. H. G. Vlooswijk, E. Snoeck, C. Magen, A. Janssens, G. Rispens, G. Rijnders, D. H. A. Blank, and B. Noheda, Nat. Mater. **10**, 963 (2011).
[20]N. T. Vo, M. Drakopoulos, R. C. Atwood, and C. Reinhard, Opt. Express **22**, 19078 (2014).
[21]T. Donath, F. Beckmann, and A. Schreyer, J. Opt. Soc. Am. A **23**, 1048 (2006).
[22]M. Guizar-Sicairos, S. T. Thurman, and J. R. Fienup, Opt. Lett. **33**, 156 (2008).
[23]D. Gürsoy, F. De Carlo, X. Xiao, and C. Jacobsen, J. Synchrotron Radiat. **21**, 1188 (2014).
[24]B. A. Dowd, G. H. Campbell, R. B. Marr, V. V. Nagarkar, S. V. Tipnis, L. Axe, and D. P. Siddons, Proc. SPIE **3772**, 224 (1999).